Geomorphology 501 (2026) 110239

Contents lists available at ScienceDirect

Geomorphology

journal homepage: www.journals.elsevier.com/geomorphology

Neck cutoff morphodynamics of compound meanders with sandy banks capped by root-reinforced layers in the Northeastern Tibetan Plateau

Yunshuo Cheng [a], Zhiwei Li [a,*], Peng Gao [b], Qunfa Zeng [a], Jiayi Ma [a]

[a] State Key Laboratory of Water Resources Engineering and Management, Wuhan University, Wuhan, Hebei, 430072, China
[b] Department of Geography and the Environment, Syracuse University, Syracuse, NY, 13244, USA

ARTICLE INFO

Keywords:
Neck breach
Compound meanders
Sandy banks
Morphodynamic feedbacks
Bar–pool topography

ABSTRACT

Neck cutoff typically occurs in highly sinuous meanders with fine-grained, cohesive banks; however, the cutoff dynamics of bends characterized by tortuous planforms and predominantly sandy bank bodies remain poorly unravelled. Black River is a major meandering river in the Zoige Basin in the Northeastern Tibetan Plateau, where sandy banks are capped by herbaceous, root-reinforced surface layers. In the lower reach, we identified two compound bends that underwent neck breach during an extreme flood, while several other regular bends remain intact. Particular focus is on bend #7, where two sub-bends at the cutoff neck show acute and broadened morphology with extremely concentrated or distributed curvature. Field surveys, aided with theoretical and numerical analysis, reveal first-order control on bend migration trajectories and cutoff timing by their tortuous geometries. Particularly, the acute bend geometry concentrates flow redistribution near the apex, promoting rapid translational migration. Conversely, broadened bend morphology attenuates local flow asymmetries, allowing the bend to remain comparatively stationary. At the final stage of neck breach, a sufficiently narrowed neck is incised by a flood extreme. We demonstrate that, for bends with sandy banks, the threshold of neck pressure-gradient can effectively distinguish flood-triggered bends from the intact ones. Compound bend morphology increases the flow-path length and thus the hydraulic gradient across the neck, enhancing both surface-flow incision and subsurface hyporheic erosion. This study advances understanding of neck cutoff dynamics in compound meanders and provides a physically based criterion for anticipating flood-induced breaching in high-altitude rivers.

1. Introduction

Neck cutoff is the terminal stage of meander evolution, where opposing limbs of a highly sinuous bend converge and intersect, forming a shorter flow path that bypasses the original loop (Constantine et al., 2010; Gao and Li, 2024). Neck cutoffs play a fundamental role in fluvial geomorphology by completing and resetting meander evolution cycles (Stølum, 1996; Constantine and Dunne, 2008; Dente et al., 2021). The elevated local slope due to shortened flow path can induce local perturbations in channel width and sediment flux that can propagate downstream, driving broader fluvial adjustments (Camporeale et al., 2008; Zinger et al., 2011; Schwenk and Foufoula-Georgiou, 2016; Weisscher et al., 2019). Also, post-cutoff changes in flow resistance and hydraulic regimes can alter flood routing dynamics, often requiring engineered interventions for effective risk mitigation (Li et al., 2021, 2025; Turnipseed et al., 2021; Zhang et al., 2022).

Numerical modeling commonly uses a geometric threshold to simulate neck cutoff triggering when the distance between meander centerlines is less than or equal to the bank width *B* (Seminara et al., 1994; Stølum, 1996). However, field investigations demonstrate a two-phase evolution. In the first stage, sustained in-bank flow causes progressive neck narrowing as adjacent limbs migrate toward one another over timescales of decades to centuries (Nanson and Hickin, 1986; Hooke, 1995; Hudson and Kesel, 2000). This gradual narrowing preconditions the neck breach by reducing flow path separation and concentrating hydraulic gradients. Finally, an episodic inundation flood with extreme intensity generates sufficient shear stress to incise a new thalweg across the narrowed neck and causes rapid channel realignment (Gay et al., 1998; Hooke, 2004).

Classically, neck cutoffs are sustained by curvature-driven migration under relatively stable hydrological regimes (such as monsoon-influenced climates) and dense arborescent riparian vegetation, which

* Corresponding author.
E-mail address: lizw2003@whu.edu.cn (Z. Li).

https://doi.org/10.1016/j.geomorph.2026.110239
Received 3 December 2025; Received in revised form 27 January 2026; Accepted 17 February 2026
Available online 19 February 2026

together promote high sinuosity and regular planform development (Ielpi et al., 2022; Finotello et al., 2024; Maitan et al., 2024; Hasson et al., 2025). In contrast, meanders evolving under sparse vegetation, flashy flow regimes, and pronounced floodplain heterogeneity commonly develop strongly asymmetric and complex planform geometries (Güneralp and Rhoads, 2011; Li et al., 2017; Cheng et al., 2025). Recent field evidence by Ielpi et al. (2021) highlights cutoff acceleration by skewed meander morphologies. However, morphodynamics of neck cutoff in bends with compound or asymmetric planforms remain underexplored, especially regarding the act of bends at extreme

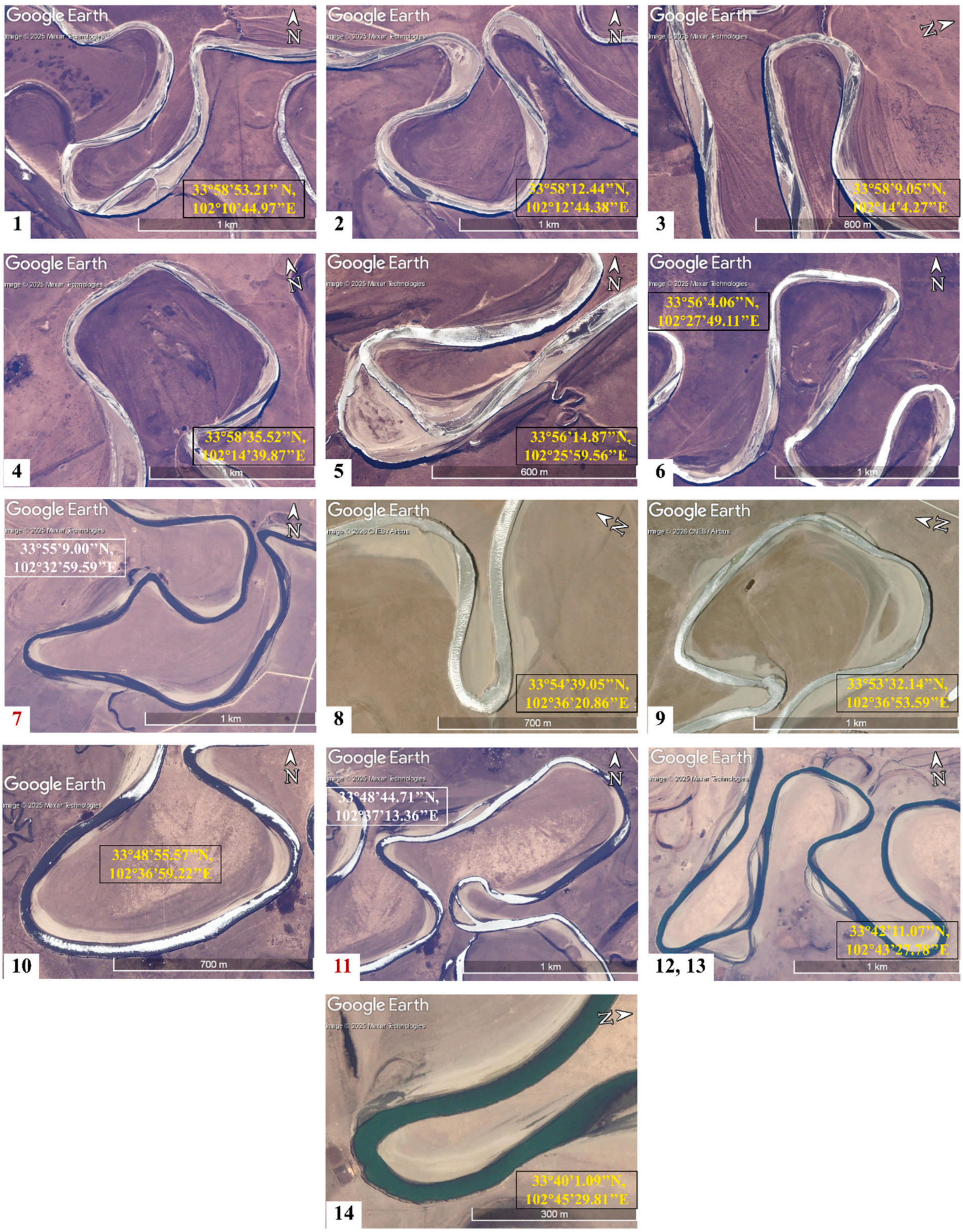

Fig. 1. Satellite images (from 2013 to 2015) of the 14 bends at the cutoff imminent stage with geological locations. Bend #7 and # 11 are marked in red, so as to highlight the cutoff occurrence during the 50-year recurrent flood in 2018. (For interpretation of the references to color in this figure legend, the reader is referred to the web version of this article.)

curvature.

The Black River (32°31′ N, 102°20′ E) is a high-sinuosity meandering river and a major tributary in the source region of Yellow River, Zoige basin, northeastern Tibetan Plateau. Regionally, fine-sediment banks are capped by herbaceous, root-reinforced surface layers. Once the lower bank is eroded, the upper layer tends to fail as coherent slump blocks that armoring the bank toe until removed by sufficiently intense episodic high flows, thereby limiting rapid bank retreat and suppressing extreme bend divergence (Parker et al., 2011; Li et al., 2023, 2025; Liu et al., 2024b). Yet interactions among non-linear bend instability, episodic high flows, and substrate heterogeneity still produce compound meander morphologies (Guo et al., 2021; Cheng et al., 2025).

In the lower Black River, 14 bends reach the near-cutoff stage with the neck width w_N less than one channel width B (Fig. 1, Li et al., 2023). Bends #7 and # 11 exhibit peculiar tortuous patterns that alternate straight reaches with locally acute or broadened sub-bends, contrasting with other bends with more regular morphologies. Bend #7 has sustained the critical condition of $w_N < 0.5B$ since the 1970s. In the summer of 2018, a 50-year recurrent flood triggered neck breach of the aforementioned two compound bends; however, several other bends remained intact, with even smaller dimensionless neck width ratios (w_N/B). This raises the central concern of the present study to reveal the two-phase neck cutoff morphodynamics in bends with compound morphologies.

In the present work, hydro-morphodynamic processes of the near-cutoff bends in the lower Black River are elucidated by combining field surveys, bed topography modeling, numerical simulations, and theoretical analysis. Particular focus is on bend #7, where a training dam was subsequently constructed at the breached neck, disconnecting the meander limbs and causing the bend to resume the pre-cutoff stage. Assessments of the pressure gradient at the neck explain the unique occurrence of the neck breach of bends #7 and #11 during the 2018 flood. This study advances the understanding of meander-cutoff dynamics in high-altitude rivers by elucidating flow–morphology interactions while introducing a predictive threshold for proactive channel management.

2. Materials and methods

2.1. Study area of the lower Black River and hydrological–hydraulic characteristics

Fig. 2a shows the satellite imagery and digital elevation model (DEM; Google Earth™) of the lower Black River Basin. The basin is characteristic of the Zoige Plateau, where broad, low-relief valley and well-developed floodplains provide ample accommodation space for channel migration and meander development. The studied reach starts from the Zoige hydrological station to the confluence with the upper Yellow River. Over a distance of ≈200 km, the channel elevation decreases by ≈23 m from 3435 m to 3412 m, yielding an average slope (S_{av}) of ≈0.12 m/km with limited local variation (Fig. 2b).

The hydrological regime of the Black River is snowmelt-driven and supplied by monsoon rainfall. Floods generally occur between June and August. The annual peak discharges at the upstream Zoige hydrological

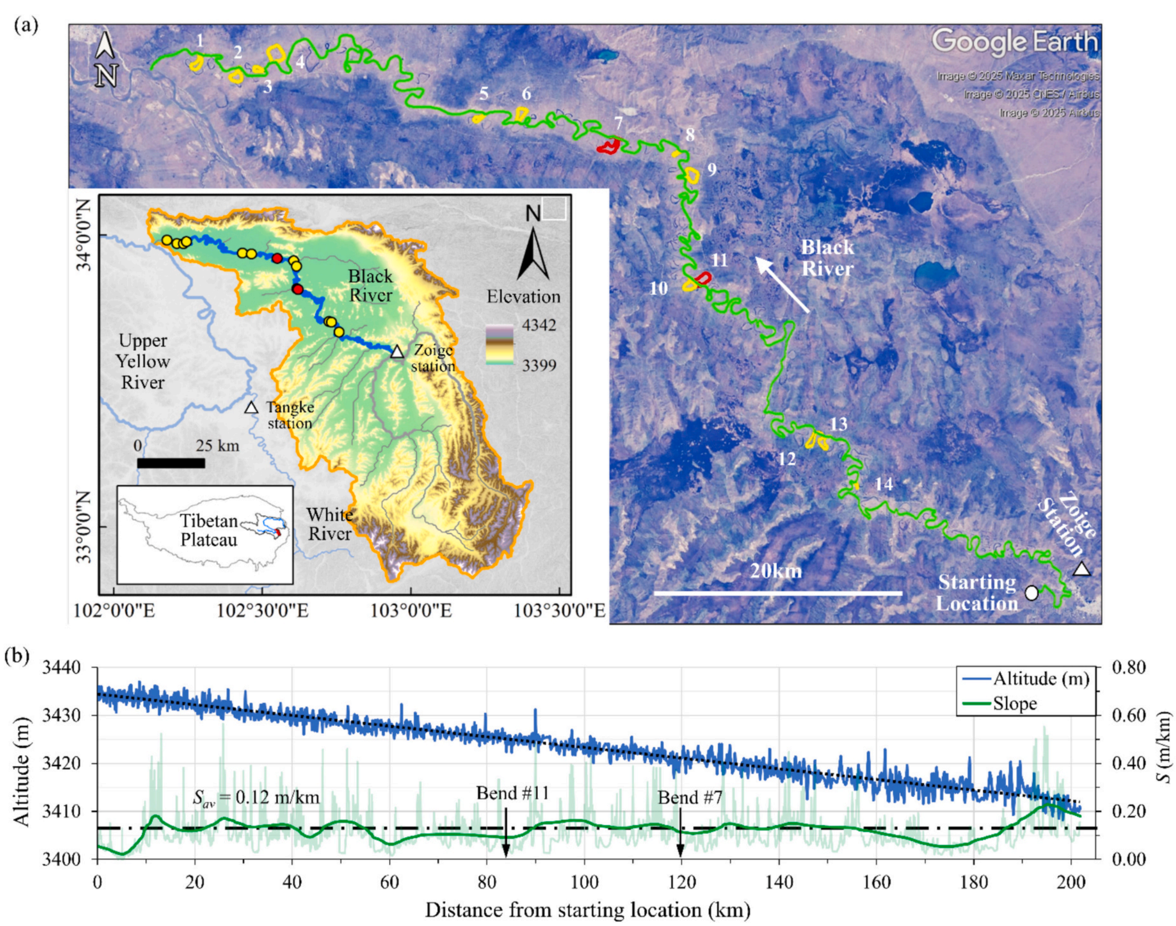

Fig. 2. An overview of the Black River in the Zoige basin. (a) Lower Black River basin with 14 near-cutoff bends. (b) Altitude and slope of the studied reach. The DEM data are obtained from Google Earth™. The shaded green curve represents the channel slope calculated using a central-difference scheme applied to longitudinal elevation data that is smoothed with a Gaussian filter using a 20 km window. These slope estimates were subsequently further smoothed and averaged over the same 20 km window to obtain the solid curve. (For interpretation of the references to color in this figure legend, the reader is referred to the web version of this article.)

station is shown in Fig. 3a.

Assuming a uniform distribution of annual precipitation and evapotranspiration across the Black River Basin, local discharges can be estimated by scaling the sub-basin area:

$$Q_L/Q_0 = A_L/A_0 \tag{1}$$

where Q_L and A_L denote the local discharge and drainage area of the sub-basin; Q_0 and A_0 correspond to those at the Zoige County hydrological Station. Sub-basin areas were delineated in Google Earth™ and subsequently calculated in ArcGIS (v.10.8.1; Supporting Fig. S1). The entire basin drains an area of 7613 km^2. The contributing area upstream of the Zoige Hydrological Station is 4560 km^2, whereas that upstream of bend #7 is 6966 km^2. Based on Eq. (1), the discharge at bend #7 is ≈1.5 times that recorded at the Zoige Station. Correspondingly, the 2-, 5-, 10-, and 50-year recurrence interval discharges at bend #7 should approximate 195, 310, 392, and 530 m^3/s, respectively (Fig. 3b).

Mean flow depth h can be estimated by combining the continuity equation ($Q = Bhu_{av}$) with Manning's equation ($u_{av} = n^{-1}\ h^{2/3}S^{1/2}$), yielding:

$$h = \left(n \cdot \frac{Q}{BS^{1/2}}\right)^{3/5} \tag{2}$$

where Q is the characteristic flow discharge, S is the channel slope (Fig. 2b), u_{av} is the mean flow velocity, and n is the Manning roughness coefficient. Based on the flood waterline, the average width B at bend #7 is approximately 64.5 m. The curve of Eq. (2) is delineated in Fig. 3b. A Manning roughness coefficient n of 0.03 (s $m^{-1/3}$) was adopted to achieve the best fit between Eq. (2) and the averaged depth measurements during three field surveys. This value of n is consistent with previously reported values, reflecting the combined influence of skin friction associated with fine-sand beds (D_{50} = 0.12 mm; Katul et al., 2002) and additional form resistance induced by strongly curved and tortuous channel geometry (Zhang et al., 2022; Lugina and Uchida, 2025). Based on this calibration, the corresponding flow depths h for the 2-, 5-, 10-, and 50-year recurrence discharge are 4.2, 5.8, 6.5, and 7.9 m, respectively (Fig. 3b).

Available records of suspended sediment concentration (SSC) from the Tangke Hydrological Station in the neighboring White River basin (Location: Fig. 2a) are used to approximate sediment conditions within the study reach (Fig. 3a). While SSC data oscillate around 0.2 g/L, the specific stream power w (= $\rho gQS/B$) associated with the 2-year recurrence flood discharge ($Q_{2\text{-}f}$ = 195 m^3/s) yields 4.5 W/m^2. This indicates a moderate energy- and sediment transport- system in the lower Black River (Nanson and Croke, 1992). Accordingly, morphodynamic adjustment (e.g., neck narrowing) during in-bank flows should be gradual, whereas substantial channel changes are primarily induced by episodic high-magnitude floods.

2.2. Field survey of bend #7

On July 12th 2018, a 50-year recurrent flood triggered neck breaches of bends #7 (Fig. 4) and #11, while other bends remained intact. At bend #7, local authorities subsequently constructed two training dams on the breached neck to regain access to the floodplain for livestock rearing. The initial earth dam failed during the flood period of 2019 (Fig. 4d). In September 2019, a rockfill embankment dam was built (275 m long, 6 m high, and 10.8 m base width), which, as of 2025, withstood multiple high-flow events. Following the construction of the second training dam, fine-grained sediment gradually accumulated at the breached neck, leading bend #7 to reverse to the near-cutoff stage (Fig. 4f). For practical purposes, the bankfull height h_{BK} is identified with the dam height, i.e., 6 m.

From 2019 to 2021, three field surveys were conducted at the upstream sub-bend of bend #7 (henceforth referred as *#7U*). The first survey was conducted on May 15th, 2019, just after the failure of the first earth dam (the neck breach stage). A total of 31 cross-sections were measured, extending from approximately 260 m upstream of the breached dam to the end of the cutoff channel (Fig. 4d). The estimated discharge was 43.5 m^3/s. The second survey was conducted one year after the second dam construction during the wet period (August 3rd, 2020) (Fig. 4e), where the estimated discharge Q was 115 m^3/s. Nine measuring cross-sections were measured this time. The final survey (July 30th, 2021) was carried out two years after the second dam construction during the dry period. The low-discharge conditions (Q = 16.4 m^3/s) caused the inner-bank point bar of *#7U* to expose above the water surface during the survey. A total of 21 cross-sections were surveyed (Fig. 4f).

During each survey, a SonTek – M9 Acoustic Doppler Current Profiler (ADCP) was installed on a SonTek Hydroboard II monohull, which can be manually pulled back and forth at roughly a constant speed. The ADCP was equipped with a nine-beam system, divided into two groups of four beams (for velocity profiles measurements with different working frequencies) and one additional vertical beam (for water depth measurement). This design ensures that the ADCP can automatically adjust to various working frequencies to optimize the sampling unit while maintaining data quality regardless of changes in water depth and

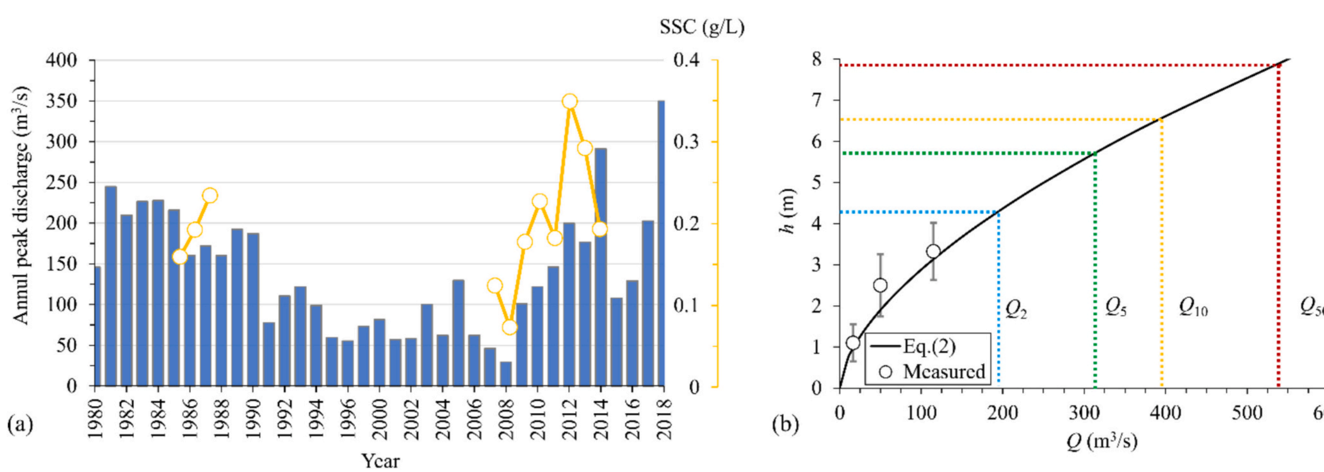

Fig. 3. (a) Hydrograph of annual peak discharge at the Zoige County hydrological station with suspended sediment concentration (SSC) at the nearby station of Tangke (location: Fig. 2a). (b) Flow depth h estimation of bend #7 through Eq. (2) (with n = 0.03 s $m^{-1/3}$), here the data are from the three field surveys with error bar denoting a standard deviation. Discharge and suspended sediment concentration (SSC) were measured using multiple verticals distributed across the cross section, with samples collected at several depths along each vertical, and subsequently integrated to obtain cross-sectional mean values.

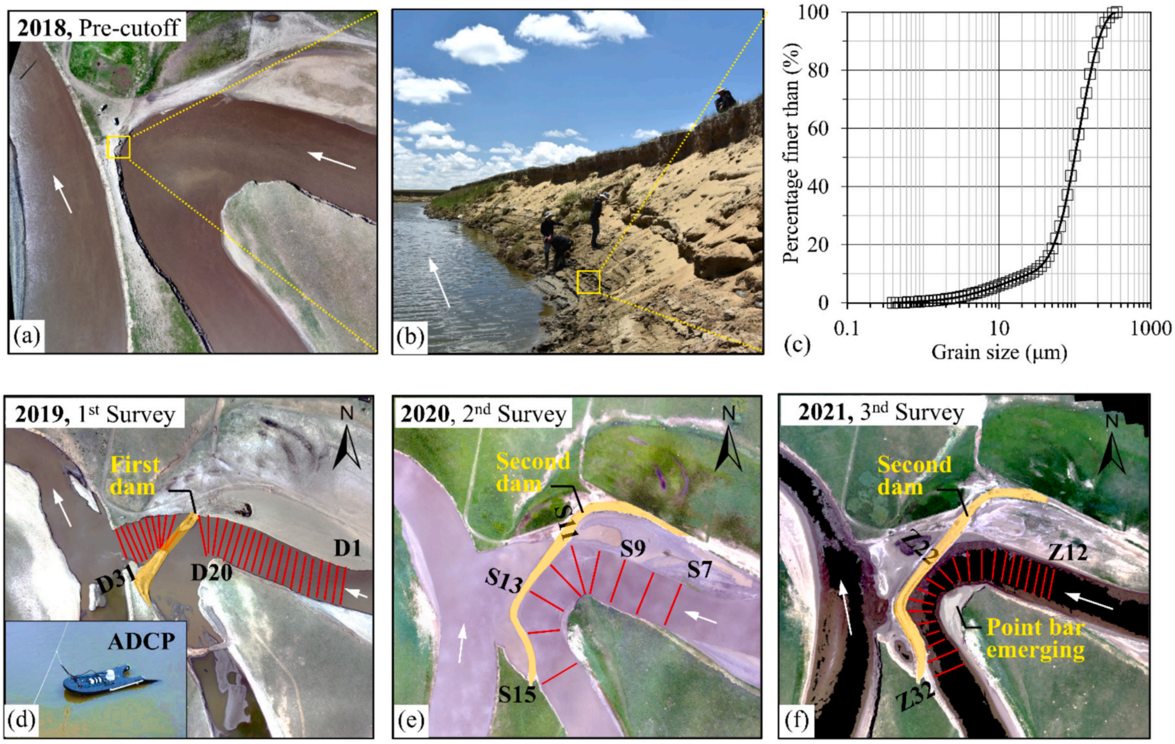

Fig. 4. Filed survey of bend #7 at different stages: (a) the narrow neck at the near-cutoff stage (in 2018); (b) outer bank of sandy body with herbaceous plat root reinforced on top; (c) sediment was sampled from the lower bank, and subsequently scanned in the laboratory and yielding D_{50} of 0.12 mm; (d–f) ADCP measurements from 2019 to 2020, from the breach of the first earth dam to 2 yr construction of the second rock embankment dam.

flow velocity. Note, velocity measurements of ADCP do not reach the channel bed due to sidelobe interference, where near-bed blanking is mandatory applied to ensure data quality. The average time interval of the ADCP measurement is 1 s, which satisfies the assumption of flow homogeneity (Szupiany et al., 2009). The position of survey lines and velocity of the monohull are recorded using an attached differential global positioning system (DGPS, Trimble R8 GNSS). The cross-sectional flow velocities and bed profiles were constructed by the River Surveyor Live software package (v.3.0) bundled with the ADCP. Since the ADCP changes the acoustic operating frequency, the accuracy of measured flow depths depends on water depth and velocity of the surveyed river channel (Konsoer et al., 2016; Moradi et al., 2019; Yuan et al., 2021). To ensure the data quality, each targeted cross-section was surveyed twice. Initial data processing and measuring error assessment are presented in Supporting Text 1.

Field surveys also confirm the two-layer structure of the banks,

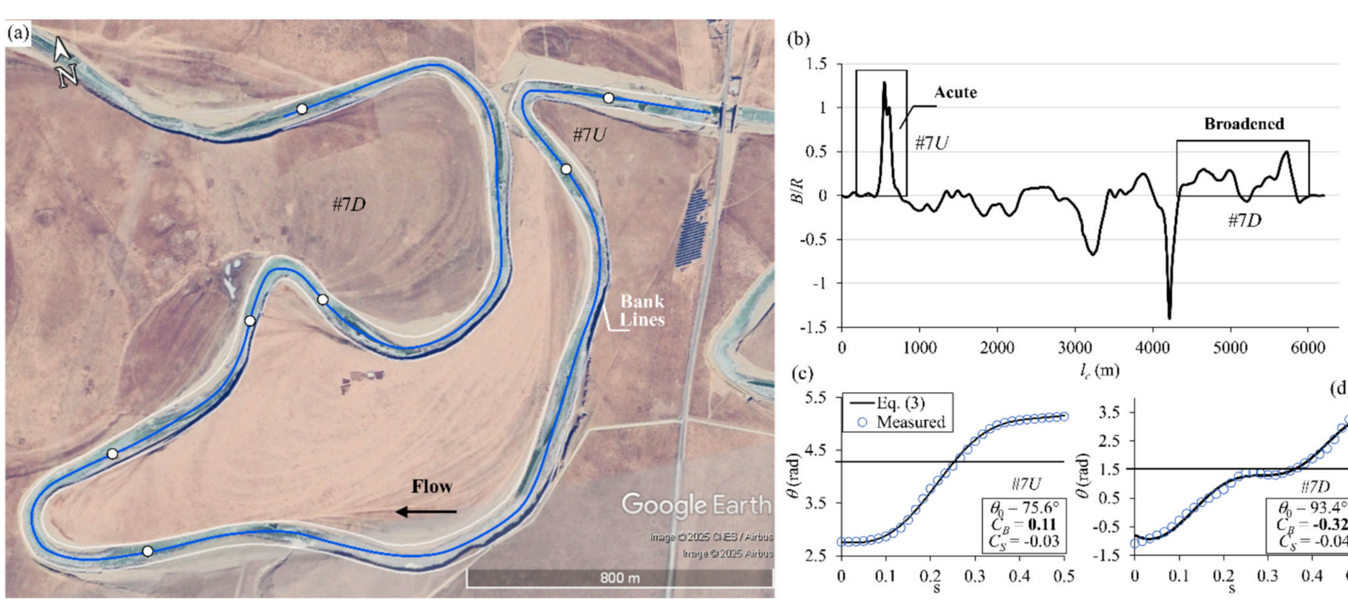

Fig. 5. Planform morphology analysis of the bend #7: (a) Satellite imagery of bend #7 at 2025 with banklines based on remnant flood lines preserved on depositional bar surfaces and incised banks; (b) distribution of dimensionless curvature B/R for the entire bend, and (c, d) fitting of the Kinoshita function to the bend angle θ at *#7U* and *#7D*.

where fine-sediment banks are capped by herbaceous, root-reinforced surface layers (Fig. 4b). Slump blocks of root-soil composite are found to scatter on eroded sloping banks or bank toes. Sediment was sampled from the lower bank and subsequently scanned in the laboratory with a laser diffraction analyser, Mastersizer 2000. The resulting grain size distribution is shown in Fig. 4c, giving a median grain size D_{50} of 0.12 mm.

2.3. Planform morphology analysis

Analysis of the planform morphology of bend #7 is presented in Fig. 5. Based on incised banks or remnant flood lines preserved on depositional bar surfaces, the banklines are delineated on the satellite image (black solid line in Fig. 5a). The channel centerline was subsequently derived from the mapped banklines and digitized to compute the bend angle θ and the dimensionless curvature B/R. Detailed procedures for calculating θ are provided in Supporting Text 3.

The curvature distribution of bend #7 is shown in Fig. 5b, highlighting contrasting planform geometries of the two sub-bends at the neck. *#7U* characterizes acute curvature concentrated over short channel lengths, whereas *#7D* exhibits broadened curvature distributed over longer lengths. To quantify this redistribution of curvature within the bend, the Kinoshita function is used to parameterize the high-order trait of each sub-bend (separated by inflections in Fig. 5a):

$$\theta = \theta_0[\cos(2\pi\cdot s) - (C_S\cdot\sin(6\pi\cdot s) + C_B\cdot\cos(6\pi\cdot s))] + c \tag{3}$$

where s is the dimensionless longitudinal coordinate along the centerline of each sub-bend (= 0 or 0.5 at inflection points), c (rad) represents the angular offset between the local system of meander coordinate (x, y) and the North-East reference frame. The third-order harmonics coefficients, C_S and C_B, quantify the effects of shifting curvature maxima or redistributing curvature within the bend, and are denoted as skewing and broadening coefficients, respectively (Cheng et al., 2025). Fitting Eq. (3) to the digitized bend angle (θ) data yields $C_B = 0.11$ for *#7U* and− 0.32 for *#7D*, confirming to the abovementioned pronounced curvature redistribution of *#7U* and *#7D*. Meanwhile, the skewing tendency is negligible.

2.4. Numerical simulations

A two-dimensional numerical model was employed to complement the limited field measurements. Specifically, the open-source numerical software TELEMAC-2D (v.8p4) is used to simulate the flow at the second survey. TELEMAC-2D solves the shallow water equations through the Finite Volume Method (Rousseau et al., 2016). Further descriptions of the numerical model are included in Supporting Text 2.

Based on the reconstructed bed topography as introduced in the following Section 3.1, an unstructured computational mesh was generated using Blue Kenue™. The mesh comprises 101,392 triangular elements with a characteristic length of 3 m. Supporting Fig. S2 presents the mesh visualization for the upstream sub-bend *#7U*. In the solution domain, measured water discharge and flow depth are imposed on the model's upstream and downstream ends, respectively, to drive the flow. The channel bed and banks were treated as non-slip rough walls, where a Manning roughness coefficient n of 0.03 (s m$^{-1/3}$) was applied (Fig. 3b). The simulation runs sufficiently long until an equilibrium state is reached. The simulated results were compared with the field measurements in Section 3.2.

2.5. Pressure gradient analysis at the cutoff neck

Neck narrowing preconditions the neck breach until an episodic inundation flood with extreme intensity incises a new thalweg across the narrowed neck and causes rapid channel realignment. To identify the physical threshold that governs this transition, we introduced a hydrodynamic-based criterion centered on head difference (Δh) between the two sides of the neck.

Considering the neck cross-section as schematically plotted in Fig. 6, the neck water surface elevation $(Z_f)_N$ during in-bank flow is given by:

$$(Z_f)_N = (Z_f)_C + \delta Z_f \tag{4}$$

where $(Z_f)_C$ is the water-surface elevation at the centerline due to the discharge conveyance (calculated via Eq. (2)), δZ_f is the tilting of the free-surface induced by the curved flow path.

At the two neck sides, the head difference (Δh) follows:

$$\begin{aligned}\Delta h &= \left[(Z_f)_N\right]_U - \left[(Z_f)_N\right]_D \\ &= \left(\left[(Z_f)_C\right]_U - \left[(Z_f)_C\right]_D\right) + \left[(\delta Z_f)_U - (\delta Z_f)_D\right]\end{aligned} \tag{5}$$

The radial water surface elevation in a curved flow can be approximated by a linear distribution (da Silva and Ebrahimi, 2017):

$$\frac{(\delta Z_f)_N}{B/2} = \frac{\partial Z_f}{\partial r} = \frac{u_{av}^2}{gR} \tag{6}$$

Assuming that (1) the channel is in a quasi-equilibrium state such that the water-surface and bed-surface centerlines are approximately parallel, and (2) bend-width variations are negligible so that the average flow depths at the two neck sides are nearly equal; the bed-elevation difference at the two neck sides can be used to approximate the water head difference along the centerline:

$$\left[(Z_f)_C\right]_U - \left[(Z_f)_C\right]_D = S\cdot L \tag{7}$$

Combining Eqs. (4)–(7) gives:

$$\Delta h = S\cdot L + \frac{Bu_{av}^2}{2g}\left(\frac{1}{R_U} - \frac{1}{R_D}\right) \tag{8}$$

The pressure gradient across the narrow neck can be obtained by normalizing the head difference (Δh) against the neck width (w_N):

$$\zeta = \frac{\Delta h}{w_N} = S\cdot\frac{L}{w_N} + \frac{B}{w_N}\cdot\frac{u_{av}^2}{2g}\left(\frac{1}{R_U} - \frac{1}{R_D}\right) \tag{9}$$

Before proceeding to the application, the physical interpretation for neck pressure–gradient ζ should be clarified. Conceptually, ζ captures the concentration of hydraulic gradient at the neck due to flow path convergence. While ζ is derived under in-bank flow conditions, we assume that during overbank flooding, the water-surface gradient of the overrun flow across the neck should scale with ζ. Thus, the higher ζ, the more likely a flood can incise and breach the narrow neck. Moreover, during in-bank flow conditions, ζ also scales the intensity of hyporheic exchange across the neck, as the studied bank constitute permeable fine sand. Enhanced hyporheic flow promotes subsurface erosion and internal weakening of the neck material, continuously undermining neck resistance and presetting the system to the eventual breach (Han and Endreny, 2014; Li et al., 2019, 2022). Overall, ζ integrates both surface-flow convergence and subsurface erosion processes, providing a physically meaningful indicator of neck vulnerability across hydrological regimes.

3. Results

3.1. Bathymetry measurements and bed topography construction

Supporting Fig. S3 shows the measured bathymetry of the upstream sub-bend (*#7U*) during the second and third field surveys. Cross-sectional profiles at critical locations (crossovers and apex) are extracted and displayed in the inset of Fig. 7. Here, the inner-bank bathymetry data during the survey of 2021 is not available due to the exposure of the inner-bank point bar during low-flow discharge. Nonetheless, it is evident that: (1) the bed topography of bend *#7U* re-established the

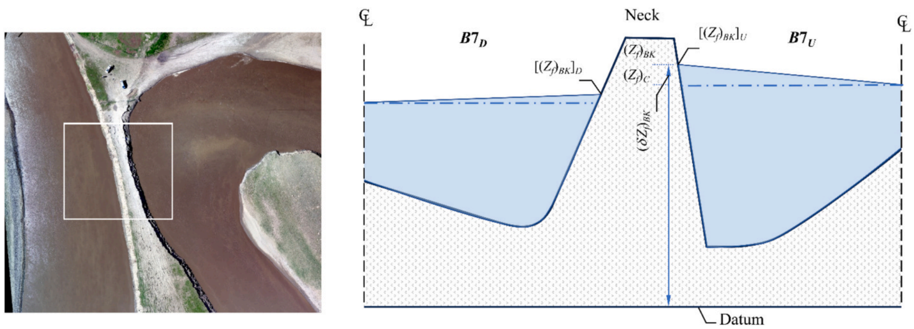

Fig. 6. A schematic plot for the assessment of the pressure gradient across the narrow neck.

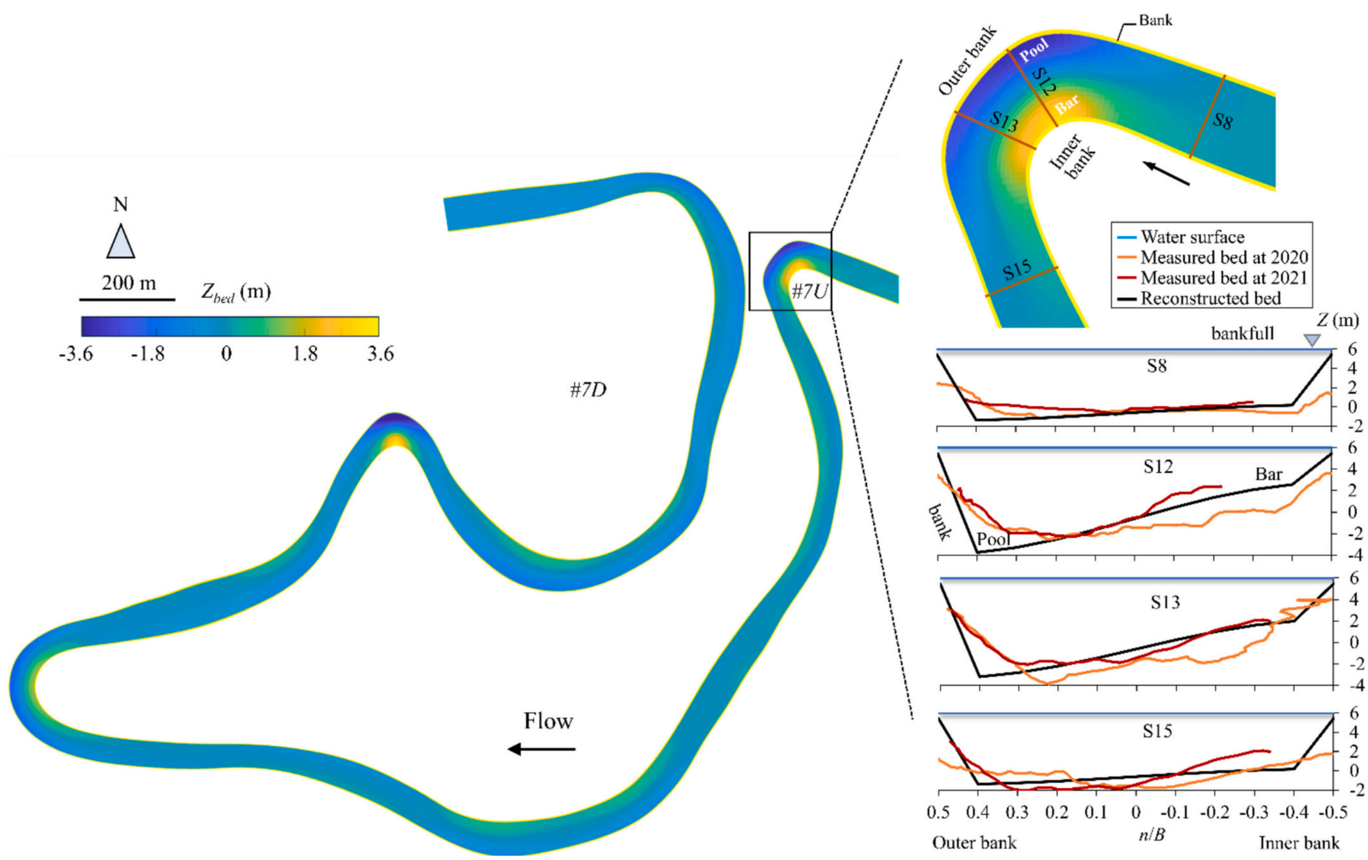

Fig. 7. Reconstructed bed topography for the model simulation and comparisons with bathymetry measurements along the upstream sub-bend *#7U*.

typical meandering point bar–pool sequence at the second survey (one year after the construction of the training dam, 2020); and (2) the inner-bank point bar continued to develop in the subsequent third survey (2021).

As is well-known, meandering bar–pool structure develops through lateral sediment balance, in which sediment transport toward the inner bank is driven by curvature-induced secondary flow, while the transverse bed-slope–induced gravitational force acts in the opposite direction (Engelund, 1974; Chen and Duan, 2006; Chen and Tang, 2012; Cheng and Li, 2024). Consequently, radial steepness of the bar–pool complexes can be estimated by (Engelund, 1974; Ikeda et al., 1981):

$$S_r = -Ah/R \tag{10}$$

where the variable h/R reflects the secondary flow intensity, and A is the scour parameter (Li and García, 2021).

Together with Eq. (10), a sinusoidal function can be used to model the bed surface (da Silva et al., 2006, da Silva and El-Tahawy, 2008):

$$\eta = \eta_c - (S_r B/2)\cdot\sin(\pi\cdot n/B) \tag{11}$$

where η is the local bed surface elevation, η_c is the bed surface elevation at the centerline, and n is the radial coordinate (= 0.5B, 0, and 0.5B at the inner bank, channel centerline, and outer bank, respectively).

The reconstructed the bed topography through combining Eqs. (10)–(11) are shown in Fig. 7 inset. The value of A = 1.0 was determined to best fit the measured bathymetry. In the near bank region (1/10B), bed elevations were made to rise linearly to the 6 m high banklines, forming a trapezoidal cross-sectional profile (Fig. 7 inset). Despite discrepancies in the outer bank (n/B = 0.3–0.5), where natural river exhibits earlier bed-to-bank transitions, the bar-pool complex at the locations of maximum curvature are realistically reproduced by the present model (S12 and S13 in Fig. 7). The same value of A is applied to build the bed topography for the entire bend #7, with the resulting contour map shown in Fig. 7.

3.2. Hydro-morphodynamics of the near-cutoff bend

In the present section, simulated velocities are validated against the field measurements (Supporting Fig. S4) to extrapolate the flow structure from the surveyed upstream sub-bend (*#7U*) to the entire bend #7. The simulated flow fields are then used to compute the centerline migration tendencies of the two sub-bends adjacent to the neck. The hydro-morphodynamic feedbacks that control neck narrowing in the pre-cutoff stage are illustrated.

Firstly, the simulated primary velocities show good agreement with the field measurements in sub-bend *#7U* (during the second survey, $Q = 115$ m^3/s). Profiles of simulated velocity fall within the error range of their measured counterparts across all cross-sections (Fig. 8). Discrepancy analysis ($= (u_{Sim} - u_{Mea})/u_{av}$, here u_{av} is the average velocity at each cross-section) along the central region ($|n/B| \leq 0.4$) indicates 70% of the data falling within the ±20% error ranges.

Importantly, our model simulation highlights divergent hydrodynamic behavior of the two sub-bends (*#7U* and *#7D*) owing to their distinct planforms (Fig. 9 inset). While the acute sub-bend *#7U* exhibits strong velocity asymmetry with the core drifting from upstream inner bank to downstream outer bank, the broadened morphology of *#7D* suppresses this velocity redistribution, developing a nearly uniform cross-stream velocity profile.

The morphological consequences of this can be estimated by considering the linear meander model by Ikeda et al. (1981):

$$\xi = E\Delta u_l \tag{12}$$

where ξ is the centerline migration rate (m/yr), E is an empirical constant that reflects the bank erodibility, and Δu_l is the primary velocity difference (m/s) between the inner and outer bank regions (i.e., $n/B = \pm 0.4$).

Comparisons between the estimated migration tendency of sub-bend *#7U* and *#7D* (based on the simulated flow fields) and historical bankline changes are presented in Fig. 10. The historical banklines are adapted from Li et al. (2023). Owing to near-uniform cross-stream velocity distribution (Fig. 9 inset), the migrating trend for the downstream sub-bend *#7D* is negligible (Fig. 10a left). The trend is confirmed by historical banklines, which shows only oscillatory shifts due to varying inundation conditions (Fig. 10b). Conversely, pronounced flow asymmetry in the acute upstream sub-bend *#7U* produces a clear translational migration tendencty toward southwest that agrees with the measured bankline changes. Furthermore, our prediction aligns more closely with these observations than the tangent-to-apex migration direction predicted by Cheng and Li (2024) from plane-bed simulations. This improvement results from the incorporation of realistic bathymetry in the present model (Section 3.1), which more accurately resolves the curvature-flow-topography feedback.

In summary, the predicted contrasting migration tendency of the two sub-bends reveals that higher-order planform geometry (bend broadness) governs local migration rates, which in turn determines the timing and likelihood of neck cutoff initiation.

3.3. Neck breach assessment

In the last stage, the neck breach is caused by an extreme inundation flood that incises a new thalweg across the narrowed neck. Comparisons in Fig. 11a and b show that the proposed criterion of neck pressure-gradient ζ ($= \Delta h/w_N$) provides a more reliable discriminator for the breach occurrence than traditional neck geometric indices. In Fig. 11a, the dimensionless neck width w_N/B, commonly used in previous studies (e.g., Li et al., 2023), does not distinguish the two bends that breached during the 2018 flood from those that remained intact. Conversely, the neck pressure gradient ζ exhibits a clear separation around a threshold value of approximately 0.012 (red dashed line; Fig. 11b), with all breached bends exceeding this threshold and all intact bends falling below it.

Sensitivity analyses in Fig. 11c and d provide additional physical insight. The neck pressure gradient ζ is largely insensitive to curvature variation across a wide range of B/R_U values, indicating that the water-

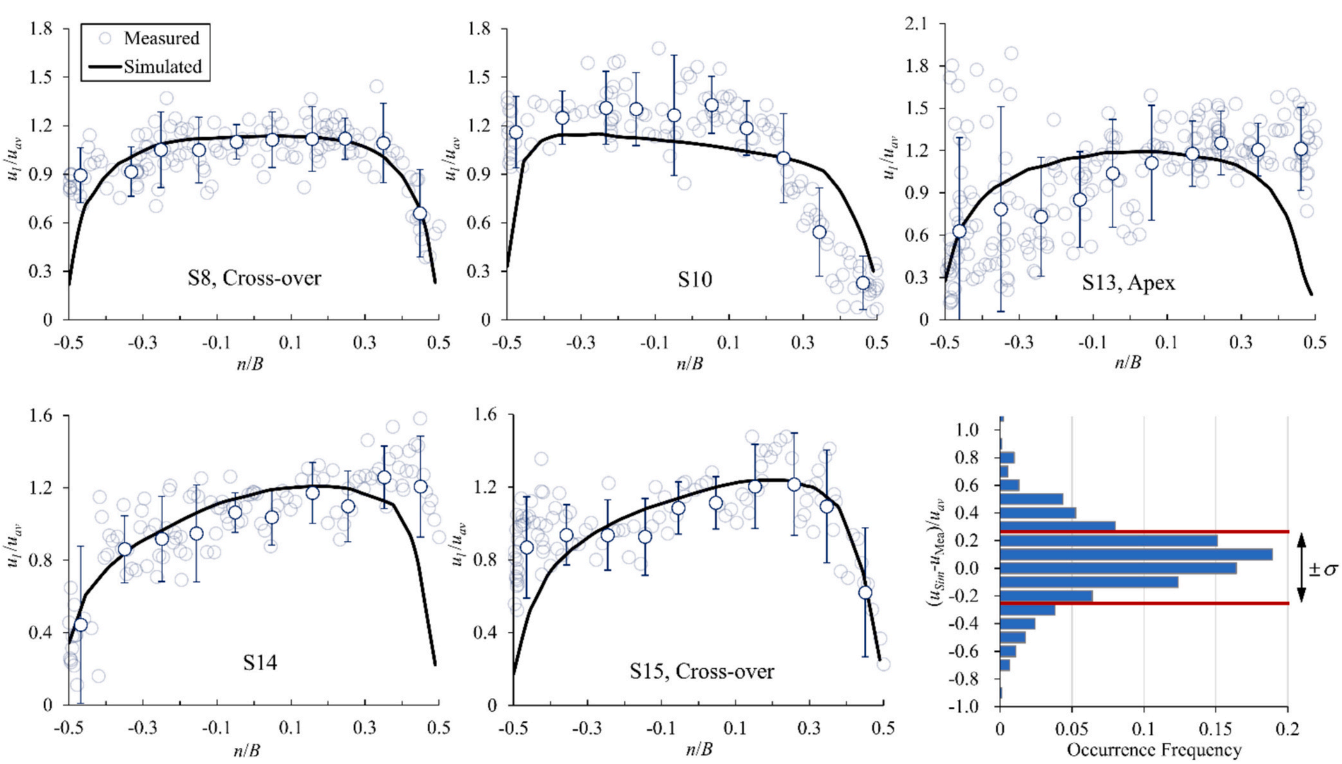

Fig. 8. Comparisons between simulated and measured primary velocities u_l for the upstream sub-bend *#7U* with occurrence frequency plot of discrepancy ($=(u_{Sim} - u_{Mea}) / u_{av}$). Here, filled circles with error bars denote the mean and 1.5σ (standard deviation) at every data bin of $\Delta n/B = 0.1$.

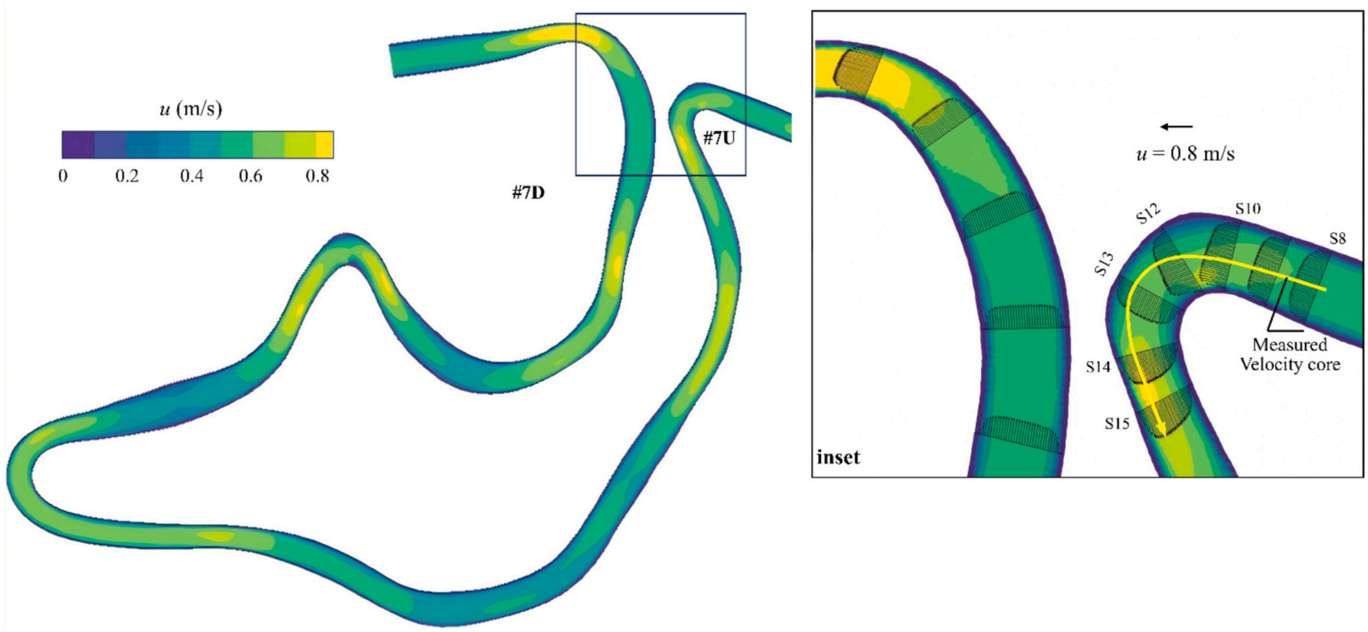

Fig. 9. Isovel plot of the simulated velocity field of the second survey pertaining to the bend in the near-cutoff stage near the bed-forming discharge, with the inset highlighting vector plots of the primary velocity (u_l) of the two sub-bends at the cutoff neck (*#7U* and *#7D*). The yellow vector line highlights the measured drifting of the velocity core from the upstream inner bank to the downstream outer bank, as adapted from Supporting Fig. S4. (For interpretation of the references to color in this figure legend, the reader is referred to the web version of this article.)

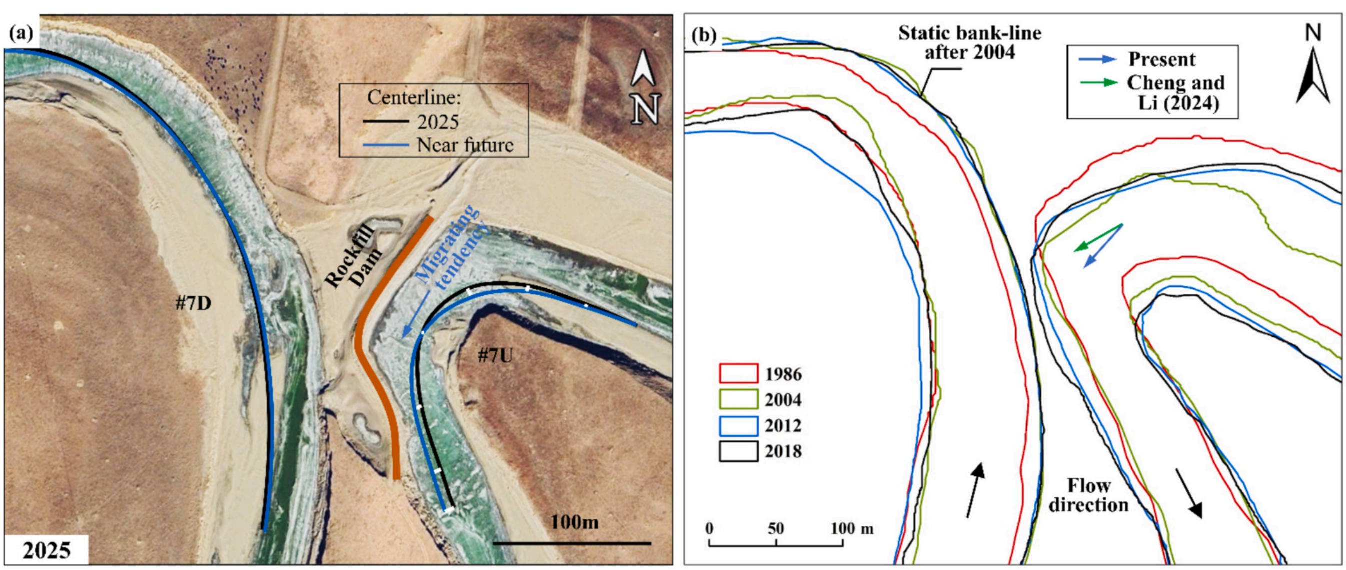

Fig. 10. Migration analysis of the two sub-bends at neck of bend #7: (a) computed centerline migrating tendencies based on simulated flow data and linear migration model of Ikeda et al. (1981), and overlayed on satellite imagery of 2025; (b) bankline changes (from satellite imagery) adapted from Li et al. (2023) that compares the present migrating tendency and that by Cheng and Li (2024).

surface tilt associated with the curved flow path does not substantially influence breach susceptibility. In contrast, ζ increases systematically with larger meander arclength L or lower normalized neck width w_N/B, highlighting the combined influence of both overall bend geometry (L) and local neck indices (w_N/B). Longer bends accumulate a larger head difference along the flow path, while a narrow neck produces a higher pressure gradient. Thus, the two bends that breached during the 2018 flood both exhibit highly compound geometries with sufficiently long meander lengths to produce the required hydraulic forcing.

4. Discussions and prospects

4.1. Meander bed topography under hydro-morpho feedbacks

The bar–pool topography of meandering streams develops under the near-bed sediment influx driven by the secondary flow. Fig. 12a depicts the vector plot of the measured secondary velocity u_r (of the second survey) at the apex cross-section (S13) of sub-bend *#7U*, showcasing the dominance of a clockwise cross-circulatory cell in the outer bank. Consider the analytical equation by Ikeda (1989):

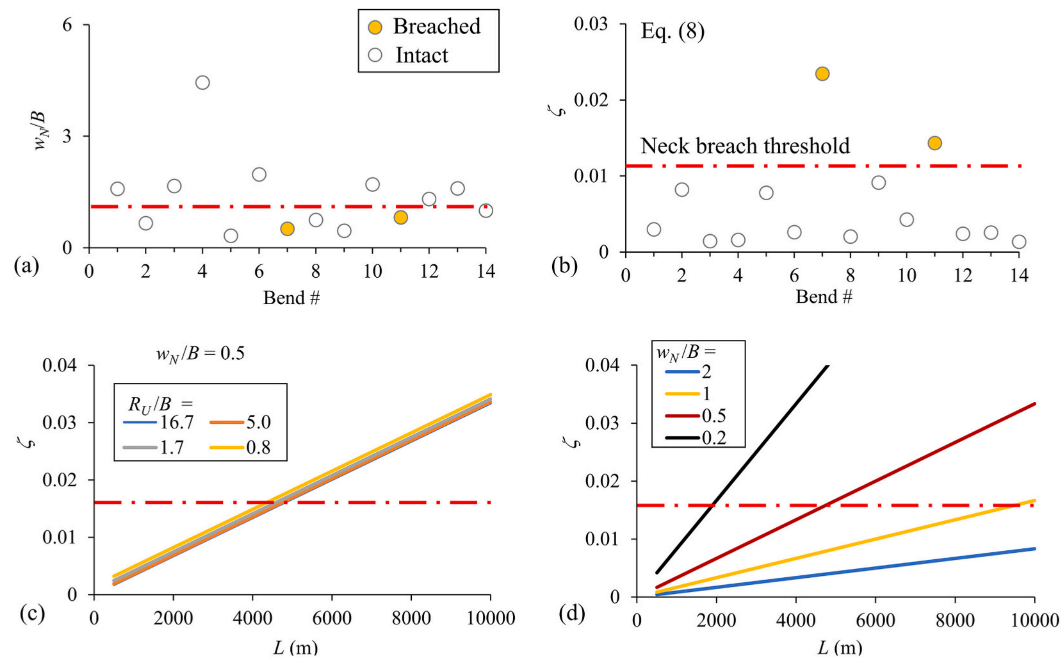

Fig. 11. Neck breach assessment for the 14 bends during the 2018 flood: (a) previous neck geometrics method; (b) present pressure-gradient criterion ζ; (c, d) sensitivity analysis of ζ regarding bend arclength L, curvature B/R_U, and neck width w_N/B.

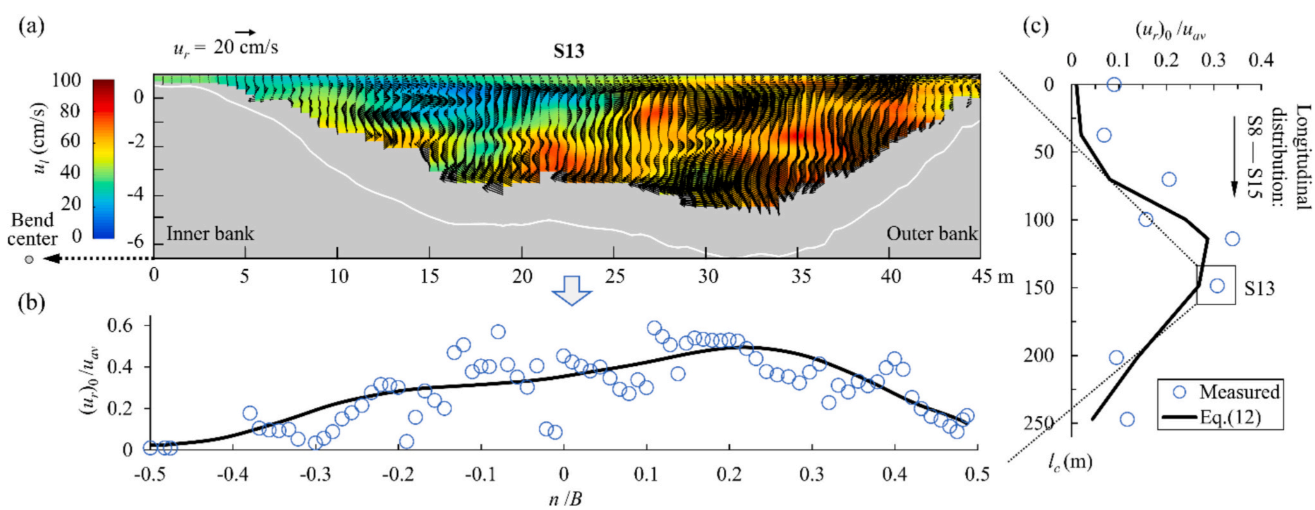

Fig. 12. Variation of the secondary velocity u_r at the upstream sub-bend *#7U*: (a) vector plot of the measured u_r at cross-section S13 along with isovel of primary velocity u_l; (b) radial and (c) longitudinal distribution of the measured near-bed radial velocity, $(u_r)_0$, along with analytical equation by Ikeda (1989).

$$\frac{(u_r)_0}{u_{av}} = \psi \cdot 7.5h\frac{r}{R^2} \tag{13}$$

where $(u_r)_0$ is the near-bed radial velocity, r is the local radius, R is the centerline radius, and ψ is the empirical coefficient that calibrates Eq. (13) with the measured data. The calibration accounts for the scale effect of natural rivers and the fact that ADCP measurements do not reach the channel bottom.

The analytical equation aligns closely with the measured data by applying $\psi = 0.5$, and captures: (1) the radial strengthening of the cross-circulatory flow toward the outer bank due to the increment of the flow depth (Fig. 12b); and (2) the longitudinal variation of the secondary flow intensity due to the centerline curvature variation (Fig. 12c).

Despite the considerable secondary-flow intensity that reaches up to 32% of the mean flow velocity (Fig. 12b), the resulting radial bed slope exhibits only moderate steepness ($A = 1$). The value falls below to those reported by Johannesson and Parker (1989; 2.6–6), Hasegawa (1989; 2–8), and Motta et al. (2014; 4–6), but aligns with the ranges documented by Chen and Tang (2012; 0–2) and Ottevanger et al. (2012; ~0.2) (see Table 1 in Li and García, 2021). Despite this broad variation and correlation with the width-to-depth ratio, we speculate that the low value of A in the present work may also reflect moderate stream power and limited suspended sediment supply of the Black River Basin (Fig. 3a). Similar scenarios have been observed in the middle and lower Yangtze River following the construction of the Three Gorges Dam, where sediment-starving conditions due to upstream sediment trapping have reduced radial bed steepness (Deng et al., 2021; Liu et al., 2024a; Yang et al., 2024; He et al., 2025).

Overall, secondary flow does not directly control bend migration because its sediment influx is counterbalanced by the transverse bed-slope–induced gravitational force (Ikeda, 1989). Instead, as discussed above, bend migration results from the combined influences of stream power conditions, suspended sediment availability, and secondary flow intensity, which together regulate the magnitude of the scouring factor A (Z. Li and García, 2021). Consequently, larger A values reflect stronger and more spatially focused flow asymmetry near the bend apex, leading to enhanced scour, accelerated migration, and earlier onset of neck narrowing (Chen and Tang, 2012).

4.2. Formation of compound bend morphology

Bends with compound morphology are more susceptible to neck breach during flood extremes because increased flow-path length amplifies hydraulic head differences across the neck. The formation of such complexity can be related to combined effects of nonlinear meander evolution, bank material heterogeneity, and strong geomorphic inheritance.

As meanders grow to finite amplitude, curvature-driven migration becomes increasingly nonlinear, allowing higher-order instabilities to develop and promoting asymmetric bend growth (Parker et al., 1983; Seminara, 2006). These instabilities are further amplified by spatial heterogeneities in bank strength, local floodplain topography, and substrate lithology, which bias erosion and deposition between neighboring bends, leading to uneven curvature redistribution and compound bend geometries (Hickin and Nanson, 1984; Hooke et al., 1990).

In the Black River, the root-reinforced surface layers modulate these processes by failing as relatively stable slump blocks that temporarily armor the bank toe and suppress rapid erosion until removed by high-discharge events (Parker et al., 2011; Li et al., 2023; Liu et al., 2024b). Although this failure mode limits extreme bend divergence, hydrodynamic instability acting within an inherited floodplain framework permits continued curvature deformation and formation of compound morphologies.

Additionally, bend #7 is situated within a reach characterized by a high density of geomorphic inheritance. The presence of at least five abandoned loops in its vicinity, formed by paleo-cutoff events, indicates repeated planform reorganization. Such clustered cutoffs disrupt the orderly progression of meander evolution by imposing inherited topographic and sedimentary constraints, further contributing to the development of tortuous, non-classical morphologies (Hooke, 2007; Frascati and Lanzoni, 2009).

4.3. Application of neck breach threshold

The proposed neck pressure-gradient ζ provides an intrinsic, process-based explanation for the occurrence of neck breach for the two compound bends, by relating effects of surface-flow incision during overbank floods and subsurface hyporheic erosion driven. However, the occurrence of breaching also depends on the intensity and cumulative effects of episodic flood inundation. Breach initiation may occur abruptly during a single extreme flood, yet field evidence also indicates that repeated overrun flows can progressively incise neck gullies, ultimately leading to the final breaching (Gay et al., 1998). Consequently, both flood magnitude and recurrence should be considered when assessing neck-breach susceptibility.

The effectiveness of the proposed threshold of neck pressure-gradient reflects the sensitivity of sandy bank bodies in the Black River to both surface erosion and subsurface hyporheic weakening. In contrast, lowland rivers with fine-grained, cohesive banks may respond differently, as bank resistance can limit hyporheic exchange and delay surface incision (Liu et al., 2024a). Evaluating the applicability and variability of the neck pressure-gradient threshold in lowland rivers with cohesive bank materials, therefore, represents an important direction for future research.

5. Conclusions

In this study, the hydro-morphodynamic controls on neck cutoff in a highly sinuous meandering river in the Northeastern Tibetan Plateau were investigated using field surveys, analytical modeling, and depth-averaged numerical simulations.

Firstly, we demonstrate that compound bend morphology exerts a first-order control on bend migration trajectories and neck cutoff timing. Acute sub-bends concentrate curvature and flow redistribution near the bend apex, promoting rapid translational migration and accelerated neck narrowing. In contrast, broadened sub-bends attenuate local flow asymmetries by redistributing curvature over longer channel lengths, thereby suppressing focused erosion and allowing bends to remain comparatively stationary even at near-cutoff stages.

For rivers with sandy banks, we show that a threshold defined by the neck pressure-gradient effectively distinguishes flood-triggered cutoffs from stable near-cutoff bends. This metric integrates the combined effects of surface-flow incision during overbank floods and progressive subsurface weakening driven by hyporheic erosion during sustained in-bank flows. Compound bend morphologies are particularly susceptible to neck breach because increased flow-path length enhances hydraulic head differences across the neck, amplifying both surface and subsurface erosional processes.

Future research should investigate how sediment supply influences the scouring factor A through targeted laboratory experiments and field observations, and should further refine the threshold value of ζ by acquiring additional field measurements and controlled experiments across diverse meandering systems.

CRediT authorship contribution statement

Yunshuo Cheng: Writing – original draft, Visualization, Validation, Methodology, Investigation, Funding acquisition, Formal analysis, Data curation, Conceptualization. **Zhiwei Li:** Writing – review & editing, Project administration, Methodology, Investigation, Funding acquisition, Formal analysis, Data curation, Conceptualization. **Peng Gao:** Supervision, Methodology, Formal analysis, Data curation, Conceptualization. **Qunfa Zeng:** Visualization, Methodology, Investigation, Data curation. **Jiayi Ma:** Visualization, Validation, Methodology, Investigation.

Declaration of competing interest

The authors declare that they have no known competing financial interests or personal relationships that could have appeared to influence the work reported in this paper.

Acknowledgements

This study was supported by the National Natural Science Foundation of China (Grant Nos. 52509109, 52479073). We sincerely thank the two anonymous reviewers for their careful evaluations and constructive comments, which have helped improve the manuscript.

Appendix A. Supplementary data

Supplementary data to this article can be found online at https://doi.org/10.1016/j.geomorph.2026.110239.

Data availability

All data supporting the findings of this study, including field measurements, bed topography model, and processed results, are available at https://doi.org/10.5281/zenodo.16554191.

References

Camporeale, C., Perucca, E., Ridolfi, L., 2008. Significance of cutoff in meandering river dynamics. J. Geophys. Res.: Earth Surf. 113, F01001.

Chen, D., Duan, J.D., 2006. Simulating sine-generated meandering channel evolution with an analytical model. J. Hydraul. Res. 44 (3), 363–373.
Chen, D., Tang, C., 2012. Evaluating secondary flows in the evolution of sine-generated meanders. Geomorphology 163, 37–44.
Cheng, Y., Li, Z.W., 2024. Morphodynamics of sine-generated meandering streams under variations of the width-to-depth ratio: A numerical investigation. J. Hydrol. 641, 131830.
Cheng, Y., Chen, D., Li, Z.W., Finotello, A., Xia, J., Gao, P., Yue, Y., He, Y., Guo, X., 2025. Scaling of river meander skewing and fattening modulated by environmental conditions. ESS Open Arch. https://doi.org/10.22541/essoar.174643358.84368181/v2.
Constantine, J.A., Dunne, T., 2008. Meander cutoff and the controls on the production of oxbow lakes. Geology 36 (1), 23–26.
Constantine, J.A., Dunne, T., Piégay, H., Mathias Kondolf, G., 2010. Controls on the alluviation of oxbow lakes by bed-material load along the Sacramento River, California. Sedimentology 57 (2), 389–407.
da Silva, A.M.F., Ebrahimi, M., 2017. Meandering morphodynamics: insights from laboratory and numerical experiments and beyond. J. Hydraul. Eng. 143 (9), 03117005.
da Silva, A.M.F., El-Tahawy, T., 2008. On the location in flow plan of erosion–deposition zones in sine–generated meandering streams. J. Hydraul. Res. 46 (sup1), 49–60.
da Silva, A.M.F., El-Tahawy, T., Tape, W.D., 2006. Variation of flow pattern with sinuosity in sine-generated meandering streams. J. Hydraul. Eng. 132 (10), 1003–1014.
Deng, S., Xia, J., Zhou, M., Li, Z., Duan, G., Shen, J., Blanckaert, K., 2021. Secondary flow and flow redistribution in two sharp bends on the middle Yangtze River. Water Resour. Res. 57 (10), e2020WR028534.
Dente, E., Lensky, N.G., Morin, E., Enzel, Y., 2021. From straight to deeply incised meandering channels: slope impact on sinuosity of confined streams. Earth Surf. Process. Landf. 46 (5), 1041–1054.
Engelund, F., 1974. Flow and bed topography in channel bends. J. Hydraul. Div. 100 (11), 1631–1648.
Finotello, A., Ielpi, A., Lapôtre, M.G., Lazarus, E.D., Ghinassi, M., Carniello, L., Favaro, S., Tognin, D., D'Alpaos, A., 2024. Vegetation enhances curvature-driven dynamics in meandering rivers. Nat. Commun. 15 (1), 1968.
Frascati, A., Lanzoni, S., 2009. Morphodynamic regime and long-term evolution of meandering rivers. J. Geophys. Res. Earth Surf. 114, F02002.
Gao, P., Li, Z., 2024. Exploring meandering river cutoffs. Geol. Soc. Lond. Spec. Publ. 540 (1), 163–184. https://doi.org/10.1144/SP540-2022-261.
Gay, G.R., Gay, H.H., Gay, W.H., Martinson, H.A., Meade, R.H., Moody, J.A., 1998. Evolution of cutoffs across meander necks in Powder River, Montana, USA. Earth Surf. Process. Landf. J. Br. Geomorphol. Group 23 (7), 651–662.
Güneralp, İ., Rhoads, B.L., 2011. Influence of floodplain erosional heterogeneity on planform complexity of meandering rivers. Geophys. Res. Lett. 38 (14), L14401.
Guo, X., Gao, P., Li, Z., 2021. Morphological characteristics and changes of two meandering rivers in the Qinghai-Tibet Plateau, China. Geomorphology 379, 107626.
Han, B., Endreny, T.A., 2014. Detailed river stage mapping and head gradient analysis during meander cutoff in a laboratory river. Water Resour. Res. 50 (2), 1689–1703.
Hasegawa, K., 1989. Universal bank erosion coefficient for meandering rivers. J. Hydraul. Eng. 115 (6), 744–765.
Hasson, M., Finotello, A., Ielpi, A., Lapôtre, M.G., 2025. Vegetation changes the trajectory of river bends. Science 389 (6763), eadv4939.
He, X., Yu, M., Wang, K., Liu, Y., 2025. Propagation of the effect of upstream bend circulations to downstream flow and sediment transport in consecutive river bends. J. Hydrol. 660, 133358.
Hickin, E.J., Nanson, G.C., 1984. Lateral migration rates of river bends. J. Hydraul. Eng. 110 (11), 1557–1567.
Hooke, J.M., 1995. Processes of channel planform change on meandering channels in the UK. In: Changing River Channels, pp. 87–115.
Hooke, J.M., 2004. Cutoffs galore!: occurrence and causes of multiple cutoffs on a meandering river. Geomorphology 61 (3–4), 225–238.
Hooke, J.M., 2007. Complexity, self-organisation and variation in behaviour in meandering rivers. Geomorphology 91 (3–4), 236–258.
Hooke, J.M., Harvey, A.M., Miller, S.Y., Redmond, C.E., 1990. The chronology and stratigraphy of the alluvial terraces of the River Dane Valley, Cheshire, NW England. Earth Surf. Process. Landf. 15 (8), 717–737.
Hudson, P.F., Kesel, R.H., 2000. Channel migration and meander-bend curvature in the lower Mississippi River prior to major human modification. Geology 28 (6), 531–534.
Ielpi, A., Lapôtre, M.G., Finotello, A., Ghinassi, M., 2021. Planform-asymmetry and backwater effects on river-cutoff kinematics and clustering. Earth Surf. Process. Landf. 46 (2), 357–370.
Ielpi, A., Lapôtre, M.G., Gibling, M.R., Boyce, C.K., 2022. The impact of vegetation on meandering rivers. Nat. Rev. Earth Environ. 3 (3), 165–178.
Ikeda, S., 1989. Sediment transport and sorting at bends. River Meandering 12, 103–125.
Ikeda, S., Parker, G., Sawai, K., 1981. Bend theory of river meanders. Part 1. Linear development. J. Fluid Mech. 112, 363–377.
Johannesson, H., Parker, G., 1989. Velocity redistribution in meandering rivers. J. Hydraul. Eng. 115 (8), 1019–1039.
Katul, G., Wiberg, P., Albertson, J., Hornberger, G., 2002. A mixing layer theory for flow resistance in shallow streams. Water Resour. Res. 38 (11), 1250.
Konsoer, K.M., Rhoads, B.L., Best, J.L., Langendoen, E.J., Abad, J.D., Parsons, D.R., Garcia, M.H., 2016. Three-dimensional flow structure and bed morphology in large elongate meander loops with different outer bank roughness characteristics. Water Resour. Res. 52 (12), 9621–9641.
Li, Z., García, M.H., 2021. A Python framework to generate synthetic riverbed topography for constant-width meandering rivers. Comput. Geosci. 152, 104755.
Li, Z.W., Yu, G.A., Brierley, G.J., Wang, Z., Jia, Y., 2017. Migration and cutoff of meanders in the hyperarid environment of the middle Tarim River, northwestern China. Geomorphology 276, 116–124.
Li, Z., Langendoen, E.J., García, M.H., 2025. Unveiling the stochasticity of bank erosion: A hybrid deterministic and stochastic modeling approach. Water Resour. Res. 61 (11), e2024WR039336.
Li, Z.W., Wu, X., Gao, P., 2019. Experimental study on the process of neck cutoff and channel adjustment in a highly sinuous meander under constant discharges. Geomorphology 327, 215–229.
Li, Z.W., Yang, H., Xia, J., Zhou, M., Deng, S., Wang, Y., 2021. Channel morphologic processes of a highly sinuous bend approaching neck cutoff by bank erosion in the middle Yangtze River. Int. J. Sed. Res. 36 (4), 457–467.
Li, Z.W., Gao, P., Wu, X., 2022. Processes of neck cutoff and channel adjustment affected by seeding herbaceous vegetation and variable discharges. Catena 208, 105731.
Li, Z.W., Gao, P., You, Y.C., Finotello, A., Ielpi, A., 2023. Delayed neck cutoff in the meandering Black River of the Qinghai-Tibet plateau. Earth Surf. Process. Landf. 48 (5), 1052–1063.
Liu, X., Xia, J., Deng, S., Zhou, M., Mao, B., Blanckaert, K., 2024a. Hydrodynamic and morphological adaptation of two consecutive sharp bends of the Middle Yangtze River to upstream damming. Water Resour. Res. 60 (1), e2023WR034990.
Liu, L., Zhu, L., Chen, D., Ran, Q., Tang, H., Yan, J., Liu, L., 2024b. Assessing the modulation of outer bank erosion by slump blocks: a case study from Marqu Meadow, China. Geomorphology 458, 109261.
Lugina, F.P., Uchida, T., 2025. The effect of channel meander on flow resistance with different aspect ratio, bed roughness, and sinuosity: fixed-flatbed cases. J. Hydrol. 666, 134864.
Maitan, R., Finotello, A., Tognin, D., D'Alpaos, A., Fielding, C.R., Ielpi, A., Ghinassi, M., 2024. Hydrologically driven modulation of cutoff regime in meandering rivers. Geology 52 (5), 336–340.
Moradi, G., Vermeulen, B., Rennie, C.D., Cardot, R., Land, S.N., 2019. Evaluation of aDcp processing options for secondary flow identification at river junctions. Earth Surf. Process. Landf. 44, 2903–2921.
Motta, D., Langendoen, E.J., Abad, J.D., García, M.H., 2014. Modification of meander migration by bank failures. J. Geophys. Res.: Earth Surf. 119 (5), 1026–1042.
Nanson, G.C., Croke, J.C., 1992. A genetic classification of floodplains. Geomorphology 4 (6), 459–486.
Nanson, G.C., Hickin, E.J., 1986. A statistical analysis of bank erosion and channel migration in western Canada. Geol. Soc. Am. Bull. 97 (4), 497–504.
Ottevanger, W., Blanckaert, K., Uijttewaal, W.S.J., 2012. Processes governing the flow redistribution in sharp river bends. Geomorphology 163, 45–55.
Parker, G., Diplas, P., Akiyama, J., 1983. Meander bends of high amplitude. J. Hydraul. Eng. 109 (10), 1323–1337.
Parker, G., Shimizu, Y., Wilkerson, G.V., Eke, E.C., Abad, J.D., Lauer, J.W., Paola, C., Dietrich, W.E., Voller, V.R., 2011. A new framework for modeling the migration of meandering rivers. Earth Surf. Process. Landf. 36 (1), 70–86.
Rousseau, Y.Y., Biron, P.M., van de Wiel, M.J., 2016. Sensitivity of simulated flow fields and bathymetries in meandering channels to the choice of a morphodynamic model. Earth Surf. Process. Landf. 41 (9), 1169–1184.
Schwenk, J., Foufoula-Georgiou, E., 2016. Meander cutoffs nonlocally accelerate upstream and downstream migration and channel widening. Geophys. Res. Lett. 43 (24), 12–437.
Seminara, G., 2006. Meanders. J. Fluid Mech. 554, 271–297.
Seminara, G., Tubino, M., Zardi, D., 1994. Planimetric Evolution of Meandering Rivers From Incipient Formation to Cutoff (in Italian), Paper Presented at XXIV Convegno di Idraulica e Costruzioni Idrauliche. Cons. Naz. Delle Ric, Naples, Italy, 20–22.
Stølum, H.H., 1996. River meandering as a self-organization process. Science 271 (5256), 1710–1713.
Szupiany, R.N., Amsler, M.L., Parsons, D.R., Best, J.L., 2009. Morphology, flow structure, and suspended bed sediment transport at two large braid-bar confluences. Water Resour. Res. 45 (5), W05415.
Turnipseed, C., Konsoer, K., Richards, D., Willson, C., 2021. Numerical modeling of two-dimensional hydrodynamics in a highly curving and actively evolving neck cutoff under different hydrologic conditions. Water Resour. Res. 57 (2), e2020WR027329.
Weisscher, S.A., Shimizu, Y., Kleinhans, M.G., 2019. Upstream perturbation and floodplain formation effects on chute-cutoff-dominated meandering river pattern and dynamics. Earth Surf. Process. Landf. 44 (11), 2156–2169.
Yang, X., Hu, Y., Sun, Z., Li, Y., Xiong, H., Li, D., 2024. Human interventions alter morphodynamics of meandering channels: insights from decadal to pre-industrial observations in the Yangtze River. J. Hydrol. 634, 131067.
Yuan, S., Tang, H., Li, K., Xu, L., Xiao, Y., Gualtieri, C., Rennie, C., Melville, B., 2021. Hydrodynamics, sediment transport and morphological features at the confluence between the Yangtze River and the Poyang Lake. Water Resour. Res. 57 (3), e2020WR028284.
Zhang, H.T., Dai, W.H., da Silva, A.M.F., Tang, H.W., 2022. Numerical study on resistance to flow in meandering channels. J. Hydraul. Eng. 148 (2), 04021059.
Zinger, J.A., Rhoads, B.L., Best, J.L., 2011. Extreme sediment pulses generated by bend cutoffs along a large meandering river. Nat. Geosci. 4 (10), 675–678.